REPORT

Cryo-EM reconstruction of a VPS13 fragment reveals a long groove to channel lipids between membranes

PeiQi Li⬤, Joshua Aaron Lees⬤, C. Patrick Lusk⬤, and Karin M. Reinisch⬤

A single particle cryo-EM reconstruction of an ~160-kD N-terminal fragment of the lipid transport protein VPS13 reveals an ~160-Å long channel lined with hydrophobic residues suitable for solubilizing multiple lipid fatty acid moieties. The structure suggests that VPS13 and related proteins, like the autophagy protein ATG2, can act as bridges between organelle membranes to allow bulk lipid flow between organelles.

Introduction

In eukaryotic cells, most membrane lipids are synthesized in the ER and then distributed to other organelles. This occurs through vesicular trafficking or else via protein-mediated lipid transport at membrane contact sites, where two organelles are closely apposed. The eukaryotic lipid transport proteins characterized so far are thought mostly to act as shuttles that extract and solubilize lipids from the membrane of the donating organelle, ferry these through the cytosol, and then deposit them in the membrane of the acceptor organelle (Wong et al., 2019). Typically, these proteins comprise domains resembling lidded tea cups, each with a hydrophobic cavity that accommodates one or two lipid molecules. Here we describe a different architecture for large proteins in the VPS13 family of lipid transporters, whose features suggest that these proteins may instead function as bridges along which bulk lipid can traverse the cytosolic space between membranes. The VPS13 proteins themselves, present in all eukaryotes, are of intense biomedical interest because their loss-of-function mutations give rise to severe neurodegenerative diseases, including chorea acanthocytosis and an early onset version of Parkinson's disease (Lesage et al., 2016; Rampoldi et al., 2001; Ueno et al., 2001). In Metazoa, they are proposed to mediate lipid exchange between the ER and mitochondria, the endolysosomal system, or lipid droplets (Kumar et al., 2018). In budding yeast, Vps13p plays a role in the biogenesis of the prospore (Park and Neiman, 2012), a double membrane structure that surrounds the four meiotic products during sporulation. Lipid transport by the VPS13-like protein ATG2 is required for the biogenesis of another double membrane structure, the autophagosome (Valverde et al., 2019).

Results and discussion

The lipid transport functionality of VPS13 resides in a ~200-kD N-terminal portion rich in β-strand structure, whereas its C-terminus is predicted to comprise a WD40 and a Pleckstrin homology domain critical in targeting the protein to organelle contact sites (Bean et al., 2018; Kumar et al., 2018). To better understand how VPS13 mediates lipid transfer, we imaged an N-terminal fragment of *Chaetomium thermophilum* VPS13, VPS13$_{1-1390}$, comprising residues 1–1390, by single particle cryo-EM, to obtain a 3D reconstruction at a nominal resolution of 3.75 Å (Fig. 1). The β-strands in VPS13$_{1-1390}$ form an extended sheet curved to resemble an open-ended basket, which is twisted by ~90° along its length. α-helices in the loops between strands trim a long edge of the basket and also assemble into a basket "handle." Because the fragment lacks a protein core, so that most side chains and long loops connecting secondary structure elements are solvent exposed and poorly resolved, it has not been possible to confidently trace the polypeptide chain. We were able to assign a Cα trace for residues 650–830 to the middle portion of the basket (shaded blue region in Fig. 1 B), which corresponds to higher resolution regions of the map. Moreover, we can definitively dock the crystal structure of the very N-terminus of the *C. thermophilum* protein, VPS13$_{1-335}$, comprising residues 1–335 (Protein Data Bank accession no. 6CBC; Kumar et al., 2018), into density at one end of the basket (Figs. 1 A and 2 A). Two helical segments (residues 99–118, disordered in 6CBC, and 300–322) were repositioned with respect to the crystal structure to form part of the basket handle (Figs. 1 A and 2 A). The VPS13$_{1-335}$ fragment is shaped like a scoop, and its concave surface is lined exclusively with hydrophobic residues (Kumar et al., 2018). Docked into the EM reconstruction, this hydrophobic surface faces the basket interior. As in this smaller fragment, the remaining β-strands in Vps13$_{1-1390}$ feature alternating hydrophobic and hydrophilic residues, and it is probable that as in the smaller fragment, the

....

Department of Cell Biology, Yale School of Medicine, New Haven, CT.

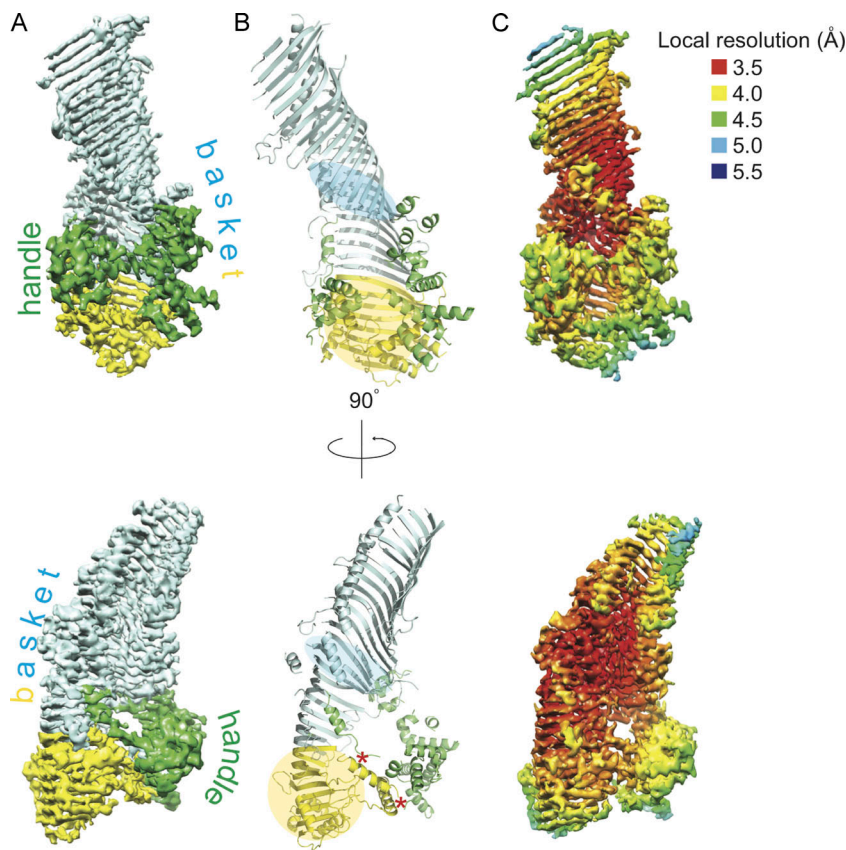Correspondence to Karin M. Reinisch: karin.reinisch@yale.edu.

Figure 1. **VPS13 forms a channel for lipid transport.** **(A)** The density map for VPS13$_{1-1390}$ (contoured at 4.55 signal/noise), which resembles a twisted gathering basket. The "basket" is colored light blue and yellow, with yellow corresponding to the portion of *C. thermophilum* VPS13 previously crystallized (Protein Data Bank accession no. 6CBC; residues 1–335). Helices comprising the "handle" are green, except for two helices from 6CBC (yellow). **(B)** Secondary structure is indicated. Red asterisks mark helices positionally adjusted with respect to 6CBC to form part of the "handle." For functional assays, mutations were introduced to render bands within the VPS13$_{1-1390}$ channel hydrophilic and unable to bind lipids. The bands are indicated in yellow (mut1) and blue (mut2) shading and arrows. **(C)** Density map colored by local resolution. In A–C, bottom: VPS13$_{1-1390}$ rotated by 90° with respect to VPS13$_{1-1390}$ in A–C, top. Top: The view is into the basket interior at the VPS13 N-terminal end. Bottom: The view is into the interior of the basket at its C-terminal end. (See also Video 1.)

hydrophobics will face the basket interior while the hydrophilics are solvent exposed. Thus, VPS13$_{1-1390}$ forms a long channel well suited for solubilizing, as reported previously (Kumar et al., 2018), tens of lipid fatty acid moieties. The hydrophilic head groups of the lipids would extrude into solvent. An interesting feature of VPS13$_{1-1390}$ is its asymmetry along its longitudinal axis: the channel is approximately twice as wide at the end harboring Vps13$_{1-335}$ as at the other, where its width across ($\sim$12 Å from Cα to Cα) resembles that of a more typical lipid transport module. A 3D cryo-EM reconstruction of ATG2, determined at $\sim$15 Å resolution, suggests that ATG2 has a long channel similar to that in VPS13$_{1-1390}$ (Valverde et al., 2019).

Like ATG2 (Chowdhury et al., 2018; Gómez-Sánchez et al., 2018; Kotani et al., 2018), VPS13 is proposed also to act as a tether, since its overexpression promotes the formation of more numerous and more extensive membrane contacts (Kumar et al., 2018; Lang et al., 2015). Via its C-terminal WD40 domain, VPS13 can interact with membrane associated proteins containing a proline-X-proline motif (Bean et al., 2018); and a FFAT motif in human VPS13A and VPS13C, which we would tentatively place in or near the "handle" in the VPS13$_{1-1390}$ reconstruction, interacts with the ER-anchored VAP protein (Kumar et al., 2018). This suggests that at contact sites VPS13 might be arranged with its length approximately normal to the membrane planes, so that lipids would access the hydrophobic cavity via its ends, one of which is formed by VPS13$_{1-335}$, and then travel between membranes through the channel (Fig. 2 B). In this "bridge" model, lipids move through the entire length of the channel, whereas in an alternative "shuttle" model, the lipids

would be stationary within the channel as the protein carries them between membranes. If the "bridge" model is correct, rendering a band within the VPS13 channel impassible to lipids, by replacing hydrophobic with hydrophilic residues unable to solubilize fatty acid moieties, should disrupt lipid transfer. If, instead, VPS13 acts as a shuttle, lipid transport should be largely unaffected by the mutations, as most of the hydrophobic channel is unaltered and would retain the ability to bind lipids. Since VPS13 function is required for prospore formation in yeast (Park and Neiman, 2012), and strains lacking the protein fail to sporulate (Enyenihi and Saunders, 2003), we tested mutant versions of VPS13 for their ability to rescue sporulation in *vps13Δ* strains. In one mutant (mut1), guided by the crystal structure, we altered a band of residues at one end of the channel in the N-terminal portion of *Saccharomyces cerevisiae* VPS13 (*vps13-mut1*: L64K/I80E/L87E/I162R/L185E/A192E/L217R/V269E/L275D/M293K/L300R; Fig. 1 B and Fig. 2, B and C). In a second mutant (mut2), based on the assignment for residues 650–830 in *C. thermophilum* VPS13, the alterations are in a band midway along the length of VPS13$_{1-1390}$ (*vps13-mut2*: V690D/L692R/L694E/I715K/A717D/M720K/I722D/I761R/I768E/F790D/M796D/L798R/V802E/I816R/G820D/L827E; Fig. 1 B and Fig. 2 B). The mutations do not interfere with folding as yeast VPS13$_{1-1350}$ constructs incorporating the mutations are monodisperse by negative stain EM, and the mutated constructs still bind lipids (Fig. S1). Furthermore, GFP-tagged full length WT and mutant constructs are expressed in yeast and localize as expected (Lang et al., 2015; Fig. 3 A and Fig. S1). Consistent with the bridge model, we found that the inability of diploid *vps13Δ* cells to sporulate could only be rescued
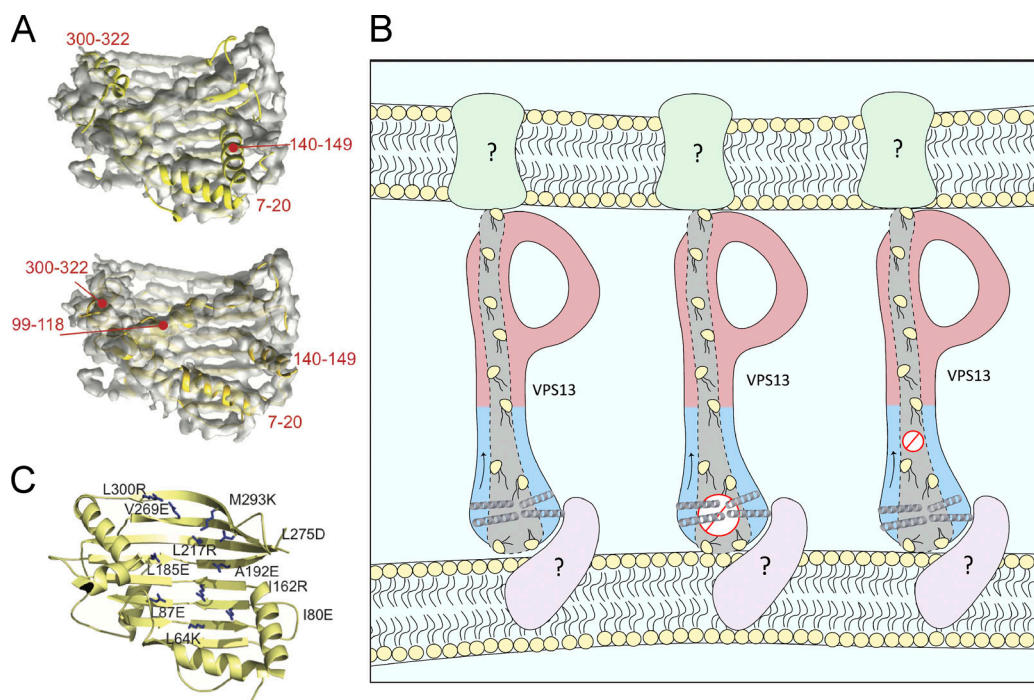
Figure 2. **The VPS13$_{1-335}$ fragment is located at the wider end of the VPS13$_{1-1390}$ "basket." (A)** VPS13$_{1-335}$ coordinates (Protein Data Bank accession no. 6CBC) were docked into the part of the EM map colored yellow in Fig. 1, A and B (top) and fitted (bottom). **(B)** VPS13 may function as a channel for lipid transfer between membranes. Intact VPS13 resembles a bubble wand (De et al., 2017); the portion corresponding to VPS13$_{1-1390}$ is blue. Mutations were introduced to render the N-terminal or middle portion of the channel hydrophilic, as indicated here and in Fig. 1 B. VPS13 may cooperate with protein partners to ensure directional lipid transport. **(C)** Changes in mut1 are indicated here in a model of *S. cerevisiae* VPS13 based on the crystal structure of Vps13$_{1-335}$ (Protein Data Bank accession no. 6CBC): L64K/I80E/L87E/I162R/L185E/A192E/L217R/V269E/L275D/M293K/L300R. Mutations in mut2: V690D/L692R/L694E/I715K/A717D/M720K/I722D/I761R/I768E/F790D/M796D/L798R/V802E/I816R/G820D/L827E.

by introduction of plasmid-borne copies of *VPS13*, but not of *vps13-mut1* or *vps13-mut2*, even when expressed from high copy number (2-μm) vectors (Fig. 3 B).

We, and others, had previously speculated that VPS13 and related proteins like ATG2 could harbor channels to facilitate the transfer of lipids between membranes (Kumar et al., 2018; Osawa et al., 2019; Valverde et al., 2019). Here we provide the first strong evidence for a continuous, hydrophobic channel in VPS13 and, by analogy, in ATG2, and a channel versus a shuttle lipid transfer mechanism. The size of the VPS13 lipid binding cavity and, hence, the ability of these proteins to accommodate many lipids simultaneously suggests a role in bulk lipid transfer. Furthermore, in the narrower, more C-terminal portions of the channel, lipids will be lined up one behind the other, indicating directional transport. Although the architecture of VPS13$_{1-1390}$ is distinct from that of other eukaryotic lipid transport modules, it broadly resembles bacterial lipopolysaccharide transporters, which feature a channel through which lipopolysaccharide travels from the inner to the outer membrane of Gram-negative bacteria (Owens et al., 2019). The bacterial channel also is a primarily β-strand structure, although composed of multiple small subunits, and resembles an open-ended basket. Importantly, it is associated with biosynthetic machinery in the inner membrane that pumps lipopolysaccharide into the channel as it is produced, thus ensuring efficient, vectorial transfer. It is tempting to speculate that this bridge-like transfer mechanism is conserved in eukaryotes, with VPS13 and ATG2 similarly collaborating with the lipid biosynthetic machinery for effective bulk lipid transfer.

The density map has been deposited in the EMDataResource (available from www.emdatabank.org under accession no. EMD-21113).

Materials and methods

Protein expression and purification

Vps13$_{1-1390}$, comprising residues 1–1390 from *C. thermophilum* Vps13, was cloned into a pCMV-10 vector containing an N-terminal 3XFLAG tag and expressed using the Expi293 Expression System (Thermo Fisher Scientific; Table S1). Cells were harvested after 95 h and resuspended in lysis buffer (50 mM HEPES, pH 7.8, 500 mM NaCl, 1 mM TCEP, and 5% glycerol supplemented with EDTA-free protease inhibitor tablet; Roche). Cells were lysed by sonication and clarified via centrifugation at 27,216 *g* for 30 min. The protein was purified by batch binding with anti-FLAG M2 Affinity Gel (Sigma-Aldrich). The resin was washed three times with five bed volumes of lysis buffer. The washed resin was incubated overnight (~15 h) with lysis buffer supplemented with 1 mM ATP and 2 mM MgCl$_2$ in a total volume of 10 ml. The resin was washed three more times, with 10 bed volumes of lysis buffer and eluted with 0.25 mg/ml of 3X FLAG peptide (APExBIO). The eluted protein was loaded onto a Superdex 200 10/300 column (GE Healthcare). The peak fractions were collected and concentrated by Amicon Ultra-4 Centrifugal
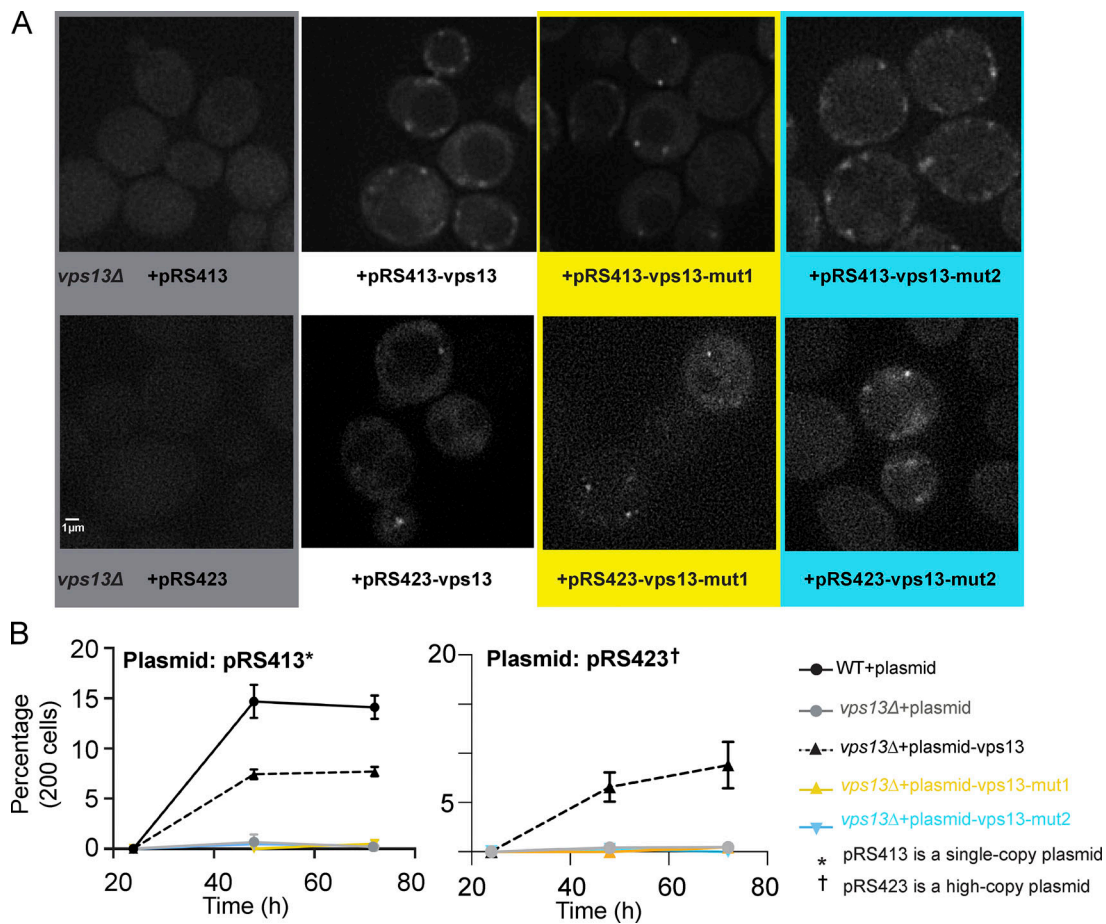
Figure 3. **Mutations that render portions of the VPS13₁₋₁₃₉₀ channel unable to bind lipids (Fig. 2, B and C) abrogate VPS13 function in sporulation.** **(A)** Low copy (*CEN*/pRS413) or multicopy (2-μm/pRS423) plasmids encoding GFP-tagged *VPS13* constructs were expressed in *vps13Δ* strains and visualized as fluorescent punctae by fluorescence microscopy. See also Fig. S1. **(B)** Yeast lacking *VPS13* fail to sporulate (Enyenihi and Saunders, 2003). Sporulation can be rescued by *VPS13* but not the channel mutants. The experiment was repeated in triplicate. SD indicated by error bars.

Filter Unit with 30-kD molecular weight cutoff. Protein at a concentration of 0.3 mg/ml was used for cryo-EM sample preparation.

Cryo-sample preparation and data collection (Table S2)
For freezing EM grids, freshly purified Vps13₁₋₁₃₉₀ was supplemented with 0.02% n-octyl-β-D-glucoside. 4 μl of sample was applied to Quantifoil R1.2/1.3 300 mesh copper grids after 30-s glow discharge. Grids were plunge-frozen in liquid ethane using an FEI Vitrobot Mark IV (Thermo Fisher Scientific) after blotting with a single blotting paper for 5 s at a blot force of –2 in 90% humidity at 4°C. Data collection was performed using an FEI Titan Krios G2 300-kV transmission electron microscope with K2 summit direct detection camera. For the first dataset, 1,976 micrographs were collected in super-resolution mode at a magnification of 135k with 1.05 Å/physical pixel with a total exposure of 8 s fractionated into 40 frames for a total dose of 50.4 e⁻/Å² with a defocus range of 1.9–2.8 μm. For the second data set, 970 micrographs were collected in super-resolution mode at a magnification of 135k with 1.05 Å/physical pixel and a total exposure of 6.2 s fractionated into 31 frames for a total dose of 49.5 e⁻/Å² with a defocus range of 1.4–2.3 μm.

Image processing (Fig. S2 and Table S2)
A total of 2,946 micrographs from two datasets were analyzed using RELION 3.0 (Zivanov et al., 2018). Super-resolution micrograph movie frames were binned by a factor of two and divided into five by five patches for motion correction by MotionCor2 (Zheng et al., 2017). Contrast transfer function estimation was done by CTFFIND-4 (Rohou and Grigorieff, 2015). Vps13₁₋₁₃₉₀ forms tail-to-tail dimers. Half of each dimer, corresponding to a monomer, was used for the 3D reconstruction. For the first dataset, 1,029 particles were manually picked from micrographs and subjected to 2D classification (Fig. S2 A). The two best 2D classes were used as references for autopicking in RELION 3.0 (Zivanov et al., 2018), which yielded a total of 564,503 particles, which were extracted using a box size of 250 × 250 pixels. For the second dataset, 506,742 particles were autopicked in RELION 3.0 (Zivanov et al., 2018) using the refined 3D map from the initial dataset to generate 2D projections as references. Particles were extracted using the same parameters as for the first dataset. For analyzing the first dataset, several rounds of 2D classification with 200 classes were used to remove ice and bad particles. An initial model was generated from 20,000 particles using stochastic gradient descent with C1

symmetry. A total of 391,836 particles were then put into 3D classification using the initial model as a reference. All the particles were classified into either three or four classes, and the best classes from these two jobs were selected separately. Particles that appeared in both classes were selected using a locally developed script and polished using Bayesian polishing in RELION 3.0 (Zivanov et al., 2018). After polishing and postprocessing, the resulting map, which was calculated from 61,230 particles, had an estimated resolution of 4.23 Å. This map was used as a reference for 3D classification for the second dataset. Following Bayesian polishing, the best final refined map from the second dataset, based on 114,134 particles, had a resolution of 3.9 Å. Polished particles from the two final maps were pooled and subjected to per-particle contrast transfer function refinement, as reported by Wan et al. (2019) and Yang et al. (2019), as implemented in RELION 3.0 (Zivanov et al., 2018). Final gold standard refinement and postprocessing were done with the resulting 175,364 particles, producing a map with an estimated resolution of 3.75 Å according to the Fourier shell correlation (FSC) = 0.143 criterion. The map was sharpened during postprocessing with a B-factor of −105.771. Local resolution estimation was performed using the RELION 3.0 (Zivanov et al., 2018) implementation.

The Vps13$_{1-335}$ crystal structure (6CBC) was docked into the map manually and fitted using UCSF Chimera (Pettersen et al., 2004). The "pseudotrace" interpreting the map in terms of secondary structure (Fig. 1 B) was built manually in Coot (Emsley et al., 2010).

Sporulation assay
Diploid vps13Δ cells were transformed with plasmids (low copy CEN/pRS413 or multicopy 2-μm/pRS423) bearing GFP-tagged versions of VPS13, vps13-mut1, and vps13-mut2 under the control of the endogenous VPS13 promoter and transferred to sporulation plates (Table S1). Sporulation efficiency was assessed by direct visualization of ascospores by light microscopy after 1, 2, and 3 d of incubation at 30°C. In these constructs, GFP was inserted after residue 499 of the VPS13 sequence, where it is known not to interfere with VPS13 function (Lang et al., 2015). Residues in the VPS13 channel were made hydrophilic in vps13-mut1 (L64K/I80E/L87E/I162R/L185E/A192E/L217R/V269E/L275D/M293K/L300R) and vps13-mut2 (V690D/L692R/L694E/I715K/A717D/M720K/I722D/I761R/I768E/F790D/M796D/L798R/V802E/I816R/G820D/L827E). Coding sequences for fragments of the genome incorporating the mutations were purchased from Genscript and replaced the VPS13 WT sequence in the mutant constructs.

Fluorescence microscopy
Yeast expressing GFP-VPS13 from a plasmid was cultured in CSM-His media with 2% of glucose at 30°C. To assess the localization of GFP-VPS13 constructs, we used a wide-field DeltaVision microscope (Applied Precision, GE Healthcare) fitted with a 100×, 1.4-NA objective (Olympus) and solid-state laser illumination. Images were acquired at 30°C using a CoolSnapHQ2 CCD camera (Photometrics) and deconvolved using the iterative algorithm in softWoRx, 7.0.0 (Applied Precision, GE Healthcare).

Immunoprecipitation
Diploid vps13Δ cells were transformed with linearized integrating plasmids (pRS406 backbone) expressing GFP-tagged versions of VPS13, VPS13-mut1, and VPS13-mut2 under the control of the GAL1 promoter using standard lithium acetate transformation methods. Yeast colonies were then streaked on selection plates containing 2% galactose and GFP expression and localization confirmed by microscopy. Selected clones were grown in 100 ml of YP media (1% yeast extract and 2% peptone) with 2% Raffinose at 30°C. A final concentration of 2% galactose was added when the cultures had reached OD$_{600}$ of 0.5. For each strain, 2 g of wet yeast pellet was resuspended with 15 ml of buffer (50 mM NaCl, 50 mM HEPES, pH 7.4, 0.1% Tween-20, 1 mM EDTA, and 1 mM PMSF) supplemented with EDTA-free protease inhibitor cocktail (Roche). Yeast were lysed by vortexing with 5-g glass beads 20 times in 30-s pulses with 1-min rests on ice in between, and the lysates were clarified via centrifugation at 27,216 g for 20 min. The protein was captured by batch binding with GFP-Trap Agarose (Chromotek). The resin was washed three times with five bed volumes of buffer. The washed resin was incubated with 6× Laemmli gel loading buffer at 95°C for 10 min and proteins were resolved on a 4%–15% gradient native gel (catalog no. 4568086; Bio-Rad).

Lipid-binding gel shift assay
3XFLAG-tagged S. cerevisiae VPS13$_{1-1350}$ with WT or mutant sequences were purified using the same strategy described above for C. thermophilum Vps13$_{1-1390}$. For lipid binding, 7 μl of 150 nM purified protein was incubated with 1 μg of dried films of NBD-phosphatidic acid, NBD-phosphatidylcholine, or no lipid on ice for 2 h. 7 μl of 2× native gel sample loading buffer was then added, and 14 μl of the sample was loaded onto a 4%–15% gradient native gel (catalog no. 4568086; Bio-Rad) and run at a constant voltage of 90 V for 90 min.

Negative staining
3XFLAG-tagged S. cerevisiae VPS13$_{1-1350}$ with WT or mutant sequences were purified using the same strategy described above for C. thermophilum Vps13$_{1-1390}$, and WT VPS13 was purified from 50 ml of Expi293 cells and mutant constructs 1 and 2 were purified from 200 ml of Expi293 cells. Samples were negatively stained on copper grids overlaid with 10-nm amorphous carbon with 2% uranyl acetate. Grids were imaged using an FEI Tecnai T12 microscope operated at an accelerating voltage of 120 kV with a nominal magnification of 52,000× (2.14 Å/pixel at the specimen level). 2D classification was performed in RELION 3.0.4, where 100 manually picked particles were selected as references for Autopick in RELION 3.0.4. Final 2D classification was done using auto-picked particles.

Online supplemental material
Fig. S1 shows the characterization of VPS13 mutant constructs. Fig. S2 shows the cryo-EM workflow. Table S1 shows the primers for the VPS13 constructs. Table S2 shows the cryo-EM data collection and image processing statistics. Video 1 shows the VPS13$_{1-1390}$ map, rotating.

References

Bean, B.D.M., S.K. Dziurdzik, K.L. Kolehmainen, C.M.S. Fowler, W.K. Kwong, L.I. Grad, M. Davey, C. Schluter, and E. Conibear. 2018. Competitive organelle-specific adaptors recruit Vps13 to membrane contact sites. *J. Cell Biol.* 217:3593–3607. https://doi.org/10.1083/jcb.201804111

Chowdhury, S., C. Otomo, A. Leitner, K. Ohashi, R. Aebersold, G.C. Lander, and T. Otomo. 2018. Insights into autophagosome biogenesis from structural and biochemical analyses of the ATG2A-WIPI4 complex. *Proc. Natl. Acad. Sci. USA.* 115:E9792–E9801. https://doi.org/10.1073/pnas.1811874115

De, M., A.N. Oleskie, M. Ayyash, S. Dutta, L. Mancour, M.E. Abazeed, E.J. Brace, G. Skiniotis, and R.S. Fuller. 2017. The Vps13p-Cdc31p complex is directly required for TGN late endosome transport and TGN homotypic fusion. *J. Cell Biol.* 216:425–439. https://doi.org/10.1083/jcb.201606078

Emsley, P., B. Lohkamp, W.G. Scott, and K. Cowtan. 2010. Features and development of Coot. *Acta Crystallogr. D Biol. Crystallogr.* 66:486–501. https://doi.org/10.1107/S0907444910007493

Enyenihi, A.H., and W.S. Saunders. 2003. Large-scale functional genomic analysis of sporulation and meiosis in Saccharomyces cerevisiae. *Genetics.* 163:47–54.

Gómez-Sánchez, R., J. Rose, R. Guimarães, M. Mari, D. Papinski, E. Rieter, W.J. Geerts, R. Hardenberg, C. Kraft, C. Ungermann, and F. Reggiori. 2018. Atg9 establishes Atg2-dependent contact sites between the endoplasmic reticulum and phagophores. *J. Cell Biol.* 217:2743–2763. https://doi.org/10.1083/jcb.201710116

Kotani, T., H. Kirisako, M. Koizumi, Y. Ohsumi, and H. Nakatogawa. 2018. The Atg2-Atg18 complex tethers pre-autophagosomal membranes to the endoplasmic reticulum for autophagosome formation. *Proc. Natl. Acad. Sci. USA.* 115:10363–10368. https://doi.org/10.1073/pnas.1806727115

Kumar, N., M. Leonzino, W. Hancock-Cerutti, F.A. Horenkamp, P. Li, J.A. Lees, H. Wheeler, K.M. Reinisch, and P. De Camilli. 2018. VPS13A and VPS13C are lipid transport proteins differentially localized at ER contact sites. *J. Cell Biol.* 217:3625–3639. https://doi.org/10.1083/jcb.201807019

Lang, A.B., A.T. John Peter, P. Walter, and B. Kornmann. 2015. ER-mitochondrial junctions can be bypassed by dominant mutations in the endosomal protein Vps13. *J. Cell Biol.* 210:883–890. https://doi.org/10.1083/jcb.201502105

Lesage, S., V. Drouet, E. Majounie, V. Deramecourt, M. Jacoupy, A. Nicolas, F. Cormier-Dequaire, S.M. Hassoun, C. Pujol, S. Ciura, et al. 2016. Loss of VPS13C function in autosomal-recessive Parkinsonism causes mitochondrial dysfunction and increases PINK1/Parkin-dependent mitophagy. *Am. J. Hum. Genet.* 98:500–513. https://doi.org/10.1016/j.ajhg.2016.01.014

Osawa, T., T. Kotani, T. Kawaoka, E. Hirata, K. Suzuki, H. Nakatogawa, Y. Ohsumi, and N.N. Noda. 2019. Atg2 mediates direct lipid transfer between membranes for autophagosome formation. *Nat. Struct. Mol. Biol.* 26:281–288. https://doi.org/10.1038/s41594-019-0203-4

Owens, T.W., R.J. Taylor, K.S. Pahil, B.R. Bertani, N. Ruiz, A.C. Kruse, and D. Kahne. 2019. Structural basis of unidirectional export of lipopolysaccharide to the cell surface. *Nature.* 567:550–553. https://doi.org/10.1038/s41586-019-1039-0

Park, J.S., and A.M. Neiman. 2012. VPS13 regulates membrane morphogenesis during sporulation in Saccharomyces cerevisiae. *J. Cell Sci.* 125:3004–3011. https://doi.org/10.1242/jcs.105114

Pettersen, E.F., T.D. Goddard, C.C. Huang, G.S. Couch, D.M. Greenblatt, E.C. Meng, and T.E. Ferrin. 2004. UCSF chimera—a visualization system for exploratory research and analysis. *J. Comput. Chem.* 25:1605–1612. https://doi.org/10.1002/jcc.20084

Rampoldi, L., C. Dobson-Stone, J.P. Rubio, A. Danek, R.M. Chalmers, N.W. Wood, C. Verellen, X. Ferrer, A. Malandrini, G.M. Fabrizi, et al. 2001. A conserved sorting-associated protein is mutant in chorea-acanthocytosis. *Nat. Genet.* 28:119–120. https://doi.org/10.1038/88821

Rohou, A., and N. Grigorieff. 2015. CTFFIND4: fast and accurate defocus estimation from electron micrographs. *J. Struct. Biol.* 192:216–221. https://doi.org/10.1016/j.jsb.2015.08.008

Ueno, S., Y. Maruki, M. Nakamura, Y. Tomemori, K. Kamae, H. Tanabe, Y. Yamashita, S. Matsuda, S. Kaneko, and A. Sano. 2001. The gene encoding a newly discovered protein, chorein, is mutated in chorea-acanthocytosis. *Nat. Genet.* 28:121–122. https://doi.org/10.1038/88825

Valverde, D.P., S. Yu, V. Boggavarapu, N. Kumar, J.A. Lees, T. Walz, K.M. Reinisch, and T.J. Melia. 2019. ATG2 transports lipids to promote autophagosome biogenesis. *J. Cell Biol.* 218:1787–1798. https://doi.org/10.1083/jcb.201811139

Wan, R., R. Bai, C. Yan, J. Lei, and Y. Shi. 2019. Structures of the catalytically activated yeast spliceosome reveal the mechanism of branching. *Cell.* 177:339–351. https://doi.org/10.1016/j.cell.2019.02.006

Wong, L.H., A.T. Gatta, and T.P. Levine. 2019. Lipid transfer proteins: the lipid commute via shuttles, bridges and tubes. *Nat. Rev. Mol. Cell Biol.* 20:85–101. https://doi.org/10.1038/s41580-018-0071-5

Yang, G., R. Zhou, Q. Zhou, X. Guo, C. Yan, M. Ke, J. Lei, and Y. Shi. 2019. Structural basis of Notch recognition by human γ-secretase. *Nature.* 565:192–197. https://doi.org/10.1038/s41586-018-0813-8

Zheng, S.Q., E. Palovcak, J.P. Armache, K.A. Verba, Y. Cheng, and D.A. Agard. 2017. MotionCor2: anisotropic correction of beam-induced motion for improved cryo-electron microscopy. *Nat. Methods.* 14:331–332. https://doi.org/10.1038/nmeth.4193

Zivanov, J., T. Nakane, B.O. Forsberg, D. Kimanius, W.J. Hagen, E. Lindahl, and S.H. Scheres. 2018. New tools for automated high-resolution cryo-EM structure determination in RELION-3. *eLife.* 7:7. https://doi.org/10.7554/eLife.42166
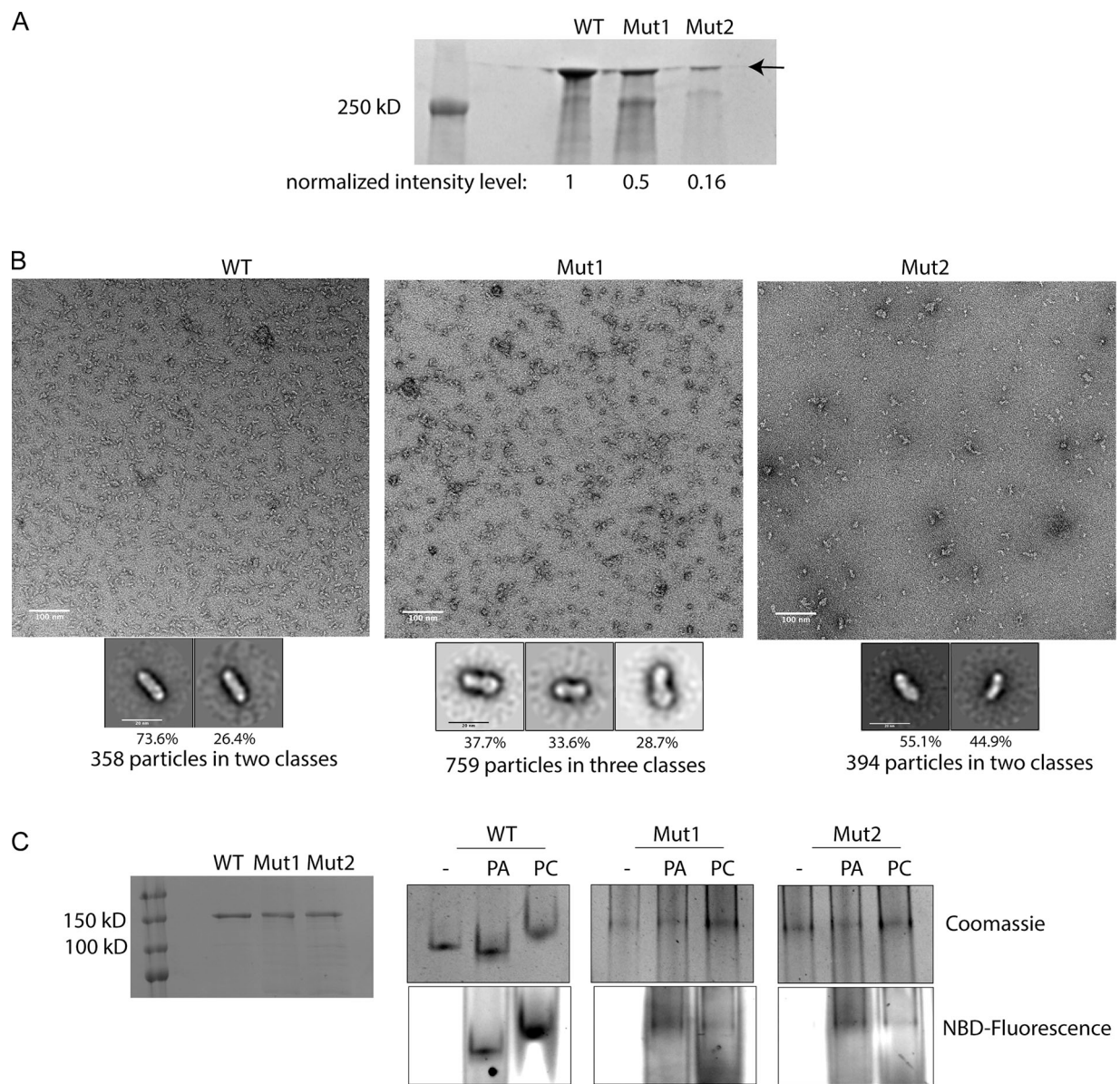
Figure S1. **Characterization of VPS13 mutant constructs. (A)** Immunoprecipitation of GFP-tagged VPS13 protein from yeast cells expressing the protein from an integrated genomic copy under control of a *GAL1* promoter. From left to right: WT, mut1, and mut2. Proteins in each lane are purified from equal numbers of cells, and the indicated yield is normalized to WT VPS13 protein. **(B)** Negative staining of 3xFLAG-tagged *S. cerevisiae* VPS13$_{1-1350}$ purified from Expi293 cells, with representative 2D-class averages shown below. Numbers of particles included in averages are indicated. From left to right: WT, mut1, and mut2. **(C)** Lipid binding gel shift assay with *S. cerevisiae* VPS13$_{1-1350}$. Equal amounts of VPS13$_{1-1350}$ constructs are coincubated with the indicated fluorescent lipids or no lipids and separated on a native gel. Gel imaging was performed both by fluorescence imaging and Coomassie staining. From left to right: WT, mut1, and mut2. PA, phosphatidic acid; PC, phosphatidylcholine.
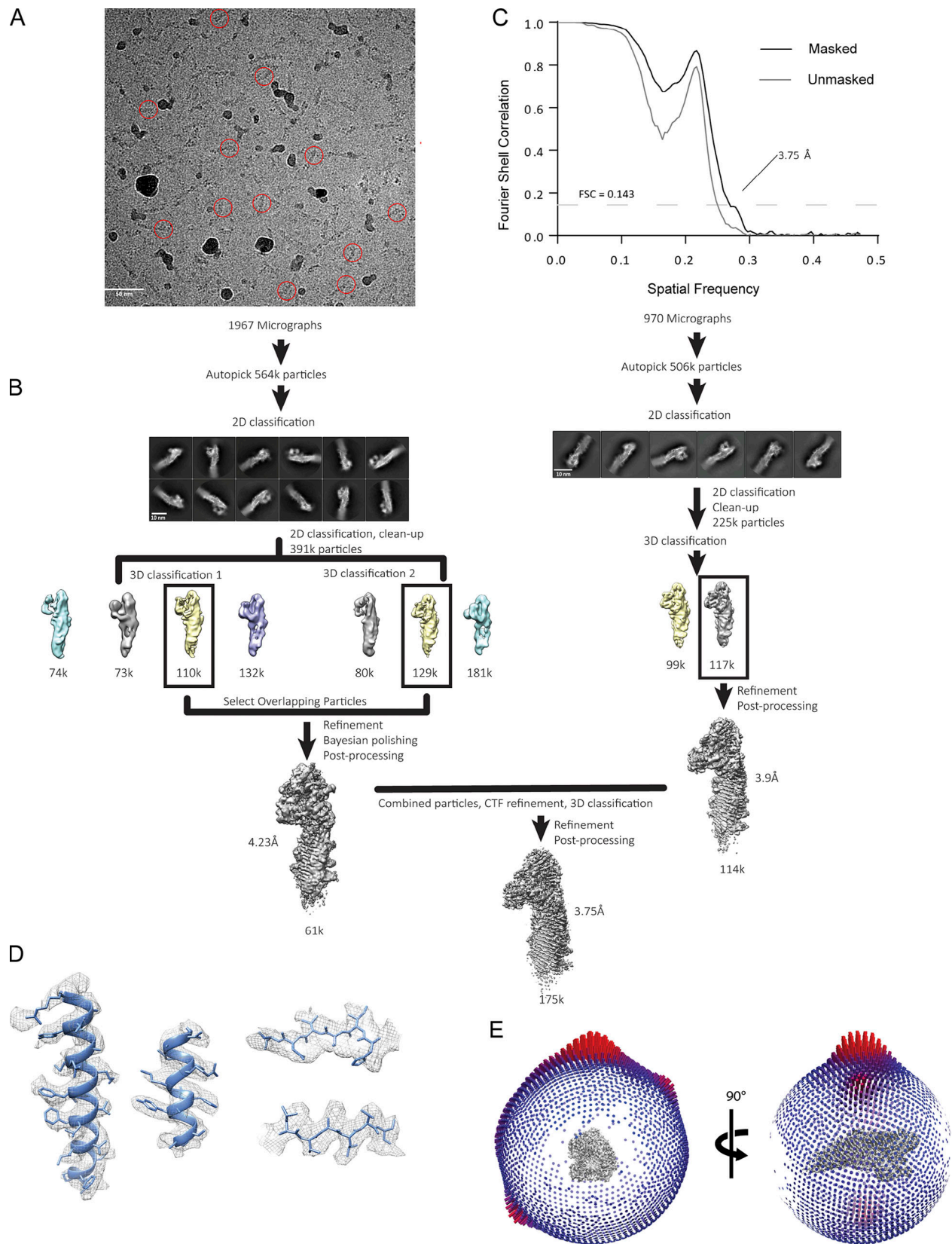
Figure S2. **Cryo-EM workflow. (A)** A representative raw micrograph of Vps13 collected on a Titan Krios. Some of the particles are circled red. See Materials and methods for details. **(B)** Cryo-EM workflow resulting in a density map at 3.75 Å resolution. The box side length of individual averages is 26.2 nm. See Materials and methods for details. **(C)** FSC curves after gold standard refinement for masked and unmasked maps with FSC cutoff at 0.143 shown by a dashed line. **(D)** Cryo-EM density for selected high-resolution regions, consistent with the reported resolution range. **(E)** Particle orientation distribution of the final map. CTF, contrast transfer function.

Video 1. **VPS13$_{1\text{-}1390}$ map.** The map of VPS13$_{1\text{-}1390}$ is rotated around the VPS13 longitudinal axis for a 3D view of the reconstruction.

Tables S1 and S2 are provided online as separate Word files. Table S1 lists the primers for the VPS13 constructs used in this study. Table S2 lists the cryo-EM data collection and image processing statistics used in this study.